Available online at www.sciencedirect.com
ScienceDirect
Journal of the European Ceramic Society 29 (2009) 3319–3332
www.elsevier.com/locate/jeurceramsoc

Nanocomposite Fe_2O_3–SiO_2 inclusion pigments from post-functionalized mesoporous silicas

M. Llusar*, V. Royo, J.A. Badenes, M.A. Tena, G. Monrós

Departament de Química Inorgànica i Orgànica, Universitat Jaume I, 12071 Castellón, Spain

Received 3 March 2009; received in revised form 15 June 2009; accepted 14 July 2009
Available online 13 August 2009

Abstract

High-surface mesoporous silicas with different pore sizes were employed for the first time as silicon precursors in the synthesis of reddish Fe_2O_3–SiO_2 inclusion pigments. Interestingly, the size of included Fe_2O_3 nanoparticles was partially controlled through confinement effects into silica mesopores. Notably, impregnated samples showed a more homogeneous and efficient encapsulation of smaller and monodisperse hematite nanoparticles (sizes around 10–35 nm). Moreover, they resulted in an improved reddish color at 1000 °C within a ceramic glaze. The best red shade ($a^* \approx 18$) was associated to nanocomposite with smaller hematite nanoparticles (around 5 nm). These promising results suggest the possibility to improve the reddish coloration and thermostability of Fe_2O_3–SiO_2 ceramic pigments through and adequate control of confinement effects into sintered mesoporous silicas.

Keywords: Nanocomposites; Porosity; Color; SiO_2; Inclusion ceramic pigments

1. Introduction

The chemical nature of inclusion (heteromorphic) pigments is based on the encapsulation of chromophore particles (normally colored transition metal oxides, such as Fe_2O_3 or V_2O_5) in the crystals of a suitable host lattice (*i.e.* SiO_2, ZrO_2 or $ZrSiO_4$).[1–5] To obtain more intense, stable and reproducible colors, it is required that the host matrix be thermostable and protect the chromophore particles against the chemical attack of the ceramic glaze to which the pigment is added.[6,7] Previous studies about inclusion ceramic pigments prepared through non-conventional chemical methods (*i.e.* coprecipitation, sol–gel and microemulsion) reveal that the coloring performance strongly depends on the microstructure of nanocomposite pigments.[8–13] An homogeneous and efficient encapsulation of chromophore oxide particles must be accomplished to obtain optimal pigmenting properties. For this purpose, it is required an accurate control of the relative sizes of chromophore and host crystals during the crystallization, sintering and inclusion processes taking place simultaneously.[1,9,10,12]

The conventional ceramic synthesis of reddish hematite–silica (αFe_2O_3–SiO_2) inclusion pigment involves the solid-state mixture and calcination (around 800–1100 °C) of appropriate Fe and Si precursors. According to previous studies,[9,14] the best reddish colorations seem to be associated to hematite crystals efficiently protected by an amorphous silica matrix. At around 1000 °C or even higher temperatures, amorphous silica crystallizes into metastable cristobalite (or also trydimite), and the resulting red shades are normally poorer. In a more recent study, however, both the thermostability and reddish color improved after cristobalite crystallization at a temperature range of 1100–1200 °C.[15] Anyway, the use of hematite–silica ceramic pigment is normally limited to low temperature ceramic glazes. In glazes with high firing temperatures (above 1000–1050 °C) the color usually becomes darker (dark brown or even grey) due to the dissolution of non-protected hematite into the glassy phase,[12,15,16] and also as a result of the partial reduction of hematite to give magnetite (Fe_3O_4).[17,18] Therefore, the thermal stability and reproducibility of this pigment are still important problems to overcome. An efficient inclusion of hematite

* Corresponding author at: Departament de Química Inorgànica i Orgànica, Universitat Jaume I, Edifici Científico-Tècnic, Av. Sos Baynat s/n, 12071 Castellón, Spain. Tel.: +34 964 728244; fax: +34 964 728214.
E-mail address: mllusar@qio.uji.es (M. Llusar).

0955-2219/$ – see front matter © 2009 Elsevier Ltd. All rights reserved.
doi:10.1016/j.jeurceramsoc.2009.07.018

particles seems to be crucial to minimize its dissolution in the glaze and also to prevent the partial reduction to magnetite.

The effect of different synthesis parameters on the coloring performance of hematite–silica red pigment has been reported in different studies. For instance, the morphology and dimensions of hematite particles can affect the red shade of pigments prepared through the coprecipitation method, depending the morphology on the precipitant agent used.[16] Also recently, Costa et al. have developed a novel approach to improve the efficiency of hematite inclusion into amorphous silica and the resulting red shade of the pigments through an innovative heterocoagulation-spray drying method.[19] Composites of iron oxides species embedded in a silica xerogel matrix have been also prepared by sol–gel methods using TEOS and different Fe salts as Si and Fe precursors, respectively. However, only the crystallochemical aspects[20,21] and magnetic properties were analyzed.[22]

The effect of surface area of silica precursor has been also analyzed.[14,15,19] In this respect, Bondioli et al. found that the red shade of the pigment obtained by the ceramic method can be slightly improved by using fine-sized colloidal (fumed) silica with higher surface area (up to 400 m^2/g).[14] Hosseini-Zori et al.[15] also reported a slight increase of the red color with increasing surface area of fumed silica. In spray-dried pigments, however, there were no evidences of different behavior with different surface areas.[19] Nevertheless, in all these studies the porous structure of precursor silicas was not analyzed, and nor its effect on the encapsulation process and final red shade of the pigments.

Chemists have now a set of efficient tools available at hand to the tailored design of a wide range of mesoporous silicas (pore sizes ranging from 2 to 50 nm).[23–28] Moreover, iron species can be homogeneously accommodated inside silica mesopores by different synthesis procedures. Indeed, after the first report of Abe et al. in 1995,[29] α-Fe_2O_3 nanoparticles and many other metal oxides (*i.e.* Ti, V, Mn, Zr, and Cu oxides) have been successfully incorporated within the inner surfaces of mesoporous silicas (MCM-41, MCM-48 or SBA-15 families). The loading of iron species can be accomplished through the use of in situ or "*one pot*" strategies.[30–39] As an alternative method, Fe species can be also incorporated within previously formed mesoporous silicas by means of "post-functionalization" routes (solid-state loading, wet impregnation, electrochemical deposition, or other post-grafting procedures).[29,33,40–51] Upon firing at high temperatures, the crystallization of hematite particles inside the voids and the adequate sintering of silica host matrix yield to an efficient hematite encapsulation.

Nevertheless, to the best of our knowledge the coloring properties and potential application of these nanocomposite systems as inclusion red pigments have not yet been investigated. Herein, we report for the first time the potential application as red ceramic pigments of hematite included in previously designed mesoporous silicas (having high surface areas and controlled pore size and pore organization). Thus, the effect of mesoporosity of silica precursor on the synthesis and coloring performance of hematite–silica ceramic pigment is analyzed. Iron incorporation within these mesoporous silicas has been carried out by solid-state loading (*route A*) and also by conventional "incipient wetness" technique (*route B*), using $FeSO_4 \cdot 7H_2O$ as iron precursor. The results are discussed in terms of the different microstructure and compared with reference ceramic samples prepared with other (non-porous) conventional silica sources (quartz and fine-sized colloidal silica).

2. Experimental procedure

2.1. Preparation of precursor mesoporous silicas

Different high-surface mesoporous silicas (see Table 1) were prepared using $Si(OCH_2CH_3)_4$ (TEOS, Fluka, 99%) and $Na_2Si_3O_7$ (sodium silicate solution, Riedel-de-Haën, 27% SiO_2, 10% NaOH) as Si sources. In order to control the mesopore size and mesoscopic organization, some commercially available templating agents were used in the synthesis: silica **1T** was prepared with an ionic surfactant (hexadecyl-trimethylammonium bromide, C_{16}TAB, from Fluka); silica **3T** was prepared with a non-ionic alkyl poly(ethylene oxide) (PEO) oligomeric surfactant ($C_{18}EO_{10}$, Brij 76, from Aldrich); finally, a poly(alkylene oxide) tri-block copolymer ($EO_{20}PO_{70}EO_{20}$, *Pluronic® P123*, $M_{av} = 5800$; from BASF) was used to obtain larger pore sizes in the synthesis of **2T** and **2S** silicas. The overall molar ratios (Si:template:EtOH:catalyst:H_2O) employed in the different preparations are summarized in Table 1. Removal of the surfactant templates after the synthesis and drying of mesoporous silicas was carried out in all cases by Soxhlet washing (with EtOH for 12 h). Washing was preferred because the proportion of non-condensed silanol groups (≡Si–OH) is expected to be considerably higher without calcination, and these moieties can then be very useful as anchoring points for the post-grafting of Fe species.

2.2. Preparation of Fe-loaded samples by post-functionalization of mesoporous silicas

Loading of Fe within the previously washed mesoporous silicas (see Scheme 1) was carried out by direct calcination (solid-state route) and also through wet impregnation (incipient

Table 1
Precursors and molar ratios used for the preparation of mesoporous silicas.

Mesoporous silica	Si precursor	Template	Catalyst	Molar ratio Si:template:EtOH:catalyst:H_2O
1T	TEOS	C_{16}TAB	HCl	1:0.18:20:0.004:5
2T	TEOS	P123	HCl	1:0.017:–:6.1:169
2S	$Na_2Si_3O_7$	P123	CH3COOH	1 (0.56Na):0.017:–:0.8:230
3T	TEOS	Brij76	HCl	1:[a]:–:3.8:128

[a] 4 g of Brij 76 were used for 8.8 g of TEOS (according to Ref. [52]).

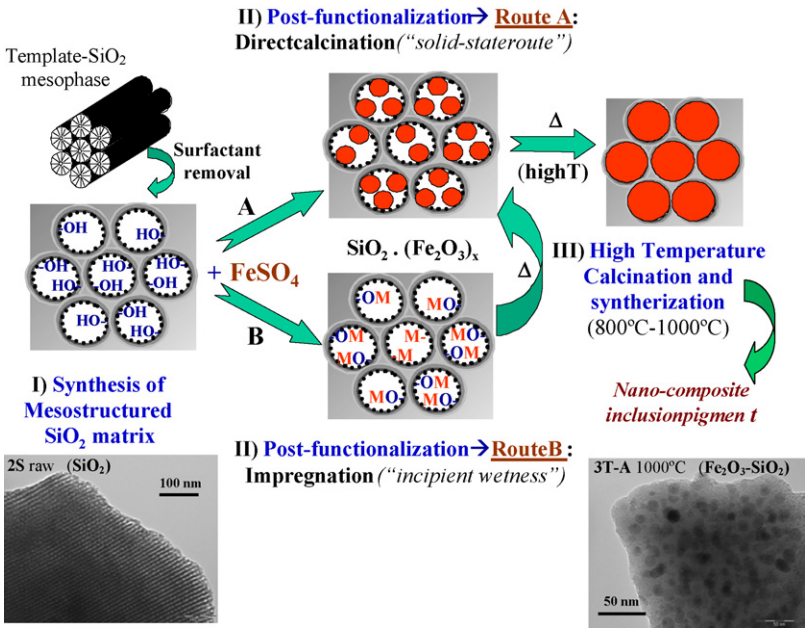

Scheme 1. Routes for the synthesis of Fe_2O_3–SiO_2 nanocomposite inclusion pigments through post-functionalization (Fe-loading) of mesoporous SiO_2 matrixes.

wetness technique). $FeSO_4{\cdot}7H_2O$ was used as iron precursor in both routes.

In the classical solid-state route (**A** samples), the formulated composition was SiO_2–$0.2Fe_2O_3$ (*ca.* 35 wt% Fe_2O_3), a typical formulation for hematite–silica pigments employed in the ceramic industry. The raw compositions were prepared by ball-milling (20 min in acetone media) stoichiometric amounts of $FeSO_4{\cdot}7H_2O$ together with the corresponding washed mesoporous silicas. To adjust the Fe:Si molar ratio to the desired composition (0.4:1), the SiO_2 content of pristine mesoporous silicas was previously estimated by differential thermal analysis (SiO_2 wt% of **1T**, **2T**, **2S** and **3T** samples around 83, 73, 86 and 81%, respectively; the DTA/TG curves are not included for brevity reasons). The obtained mixtures were air-dried at room temperature (for complete acetone evaporation) and then fired in an electric furnace (in air) up to two different temperatures (800 and 1000 °C). The firing schedule consisted of heating in 4 h up to 800 or 1000 °C, soaking times of 2.5 h at this temperature, and a free cooling down to room temperature.

In the wet impregnation route (**B** samples), the host mesoporous silicas were Fe-loaded by the *incipient wetness* technique[33,40,41,44,45,48–50] with a 0.7 M aqueous solution of iron(II) sulphate at a pH of *ca.* 2. In a typical impregnation experiment, mesoporous silicas were suspended and vigorously stirred (at room temperature for 1 h) in the aqueous iron solution (25 mL of solution for 1 g of silica), repeating this process two times. After the third impregnation cycle, the powders were suspended in deionized water also at room temperature for 1 h and then dried at 80 °C. This suspension treatment has been confirmed to favor the migration of Fe ions loaded on the outer surface into the pores.[29,41] The as-loaded Fe–SiO_2 composites were then fired (this time only up to 1000 °C) following the same firing schedule as with **A** samples (4 and 2.5 h of heating and soaking times, respectively).

For comparison reasons, two conventional ceramic references (**R1** and **R2**) with the same commercial composition (SiO_2–$0.2Fe_2O_3$) were also prepared by ball-milling the corresponding amounts of hydrated iron sulphate and two conventional silicon sources. The employed SiO_2 precursors were a commercial quartz from ATC (95% SiO_2, 4 m^2/g of surface area) in **R1** sample, and a fine-sized colloidal silica from Salquisa (76% SiO_2, 107 m^2/g of surface area) in **R2** sample.

2.3. Characterization techniques

Simultaneous differential thermal and thermo-gravimetric analysis (DTA–TGA) of washed mesoporous silicas was carried out with a Mettler Toledo thermal analyzer (using Pt crucibles with a constant 5 °C/min heating from 25 up to 1100 °C). The porosity of mesoporous silicas (after Soxhlet washing) was characterized by the conventional nitrogen adsorption–desorption method at −196.15 °C using an ASAP 2010 (Micrometrics Co.) analyzer. The samples were outgassed in vacuo at 150 °C for 12 h, prior to each measurement. Specific surface areas were obtained by using the BET equation between 0.05 and 0.30 relative pressures,[53–55] and pore size distributions were determined by the BJH method for mesopores.[56]

Conventional powder X-ray diffraction (XRD) of calcined samples was performed with a Siemens D-500 Diffractometer with Ni-filtered CuK_α radiation (from 10° to 60° 2θ, with steps of 0.02° 2θ and a counting time of 2 s at each step). The morphology and microstructure of nanocomposites were examined by scanning electron microscopy (SEM) with a Leo-440i Leyca electron microscope (as grain mounts following conventional preparation and imaging techniques). Semiquantitative elemental analysis (Si:Fe molar ratio and mapping distribution) was obtained with an EDX analyzer attached to the microscope and supplied by Oxford University. Further microstructure details

Table 2
Structural parameters of mesoporous silicas after Soxhlet washing (BET surface area, pore volume, pore size (BJH), and characteristic *d* spacing).

Mesoporous silica	BET surface area, S_{BET} (m^2/g)	Pore volume, V_t (cm^3/g)	Pore size (BJH)[a], D_{BJH} (nm)	*d* spacing[b], *d* (nm)
1T	1114	0.91	2.7	5.0
2T	647	0.92	7.1	11.8
2S	629	0.95	7.0	11.9
3T	640	0.54	3.3	5.7

[a] Average pore size (D_{50}) calculated from BJH size distribution curves (desorption branch).
[b] *d* (1 0 0) spacing (for **2T** and **2S**) or characteristic reflection (for **1T** and **3T**) obtained from small-angle X-ray diffraction (SAXRD) measurements (figure not included for brevity reasons).

were obtained by transmission electron microscopy (TEM) in a JEOL JEM-1010 (100 kV) microscope. For TEM observations, the micronized powders were suspended in EtOH, and deposited after sonication onto conventional holey carbon grids.

In order to test their coloring performance as reddish ceramic pigments the obtained nanocomposites were 5 wt% enameled with a commercial double-firing transparent glaze (approximate Seger formula: K_2O 0.106, CaO 0.565, ZnO 0.329, Al_2O_3 0.323, SiO_2 1.972) onto conventional (fired) ceramic biscuits, and fired following a fast-firing scheme (60 min of duration from cool to cool at a maximum temperature of 1085 °C). The optical and/or coloring properties of enameled samples were analyzed by UV–vis–NIR spectroscopy (diffuse reflectance) performed with a PerkinElmer (lambda 2000) spectrophotometer at a range between 300 and 1000 nm. Color parameters ($L^*a^*b^*$) were also measured using a standard lighting C, following the CIE-L*a*b* colorimetric method recommended by the CIE (Commission Internationale de l'Eclairage).[57] On this method, L^* is the lightness axis (black (0) → white (100)), b^* is the blue (−) → yellow (+) axis, and a^* is the green (−) → red (+) axis.

3. Results and discussion

3.1. Characterization of templated mesoporous silicas

The results obtained in the BET/BJH characterization of Soxhlet-washed mesoporous silicas are summarized in Table 2. Nitrogen adsorption–desorption isotherms (BET method) and pore size distribution curves (BJH method) are also shown in Fig. 1. As may be appreciated, mesoporous silica **1T** (prepared with surfactant C_{16}TAB) presents the highest surface area of all silicas (around 1114 m^2/g), associated to very small pore sizes. The BJH distribution curve shows a relatively broad distribution of small pore sizes (average pore size around 2.7 nm; the average pore sizes –D_{BJH} – were estimated in all cases from the BJH desorption branches). In comparison, mesoporous silica **3T** (prepared with non-ionic surfactant Brij 76), presents a smaller surface area (640 m^2/g) and pore volume. Attending to the BJH curve, the mesoporous framework of **3T** sample is constituted by slightly larger (average D_{BJH} around 3.3 nm) and acceptably monodisperse mesopores. On the other hand, mesoporous silicas **2T** and **2S** (prepared with tri-block copolymer *Pluronic® P123*) contain considerably larger mesopores (type IV isotherm),[55] as it was expected. The BJH curves of these two samples are clearly indicative of a monodisperse pore size distribution (average D_{BJH} around 7.1 and 7.0 nm for **2T** and **2S**, respectively). Despite of the high physisorption, the BET surface areas of **2T** and **2S** mesoporous silicas (around 647 and 629 m^2/g) are very similar to sample **3T** and considerably smaller than in **1T**.

Finally, TEM characterization allowed us to corroborate and complement the previous BET/BJH results (see representative TEM details of washed mesoporous silicas in Fig. 2). TEM observations reveal that sample **1T** contains a rather disordered (amorphous), wormlike mesoporosity (Fig. 2a) with very small pore sizes (approximately below 5 nm). In contrast, mesoporous silicas **2T** and **2S** consist of well-organized and larger mesopores

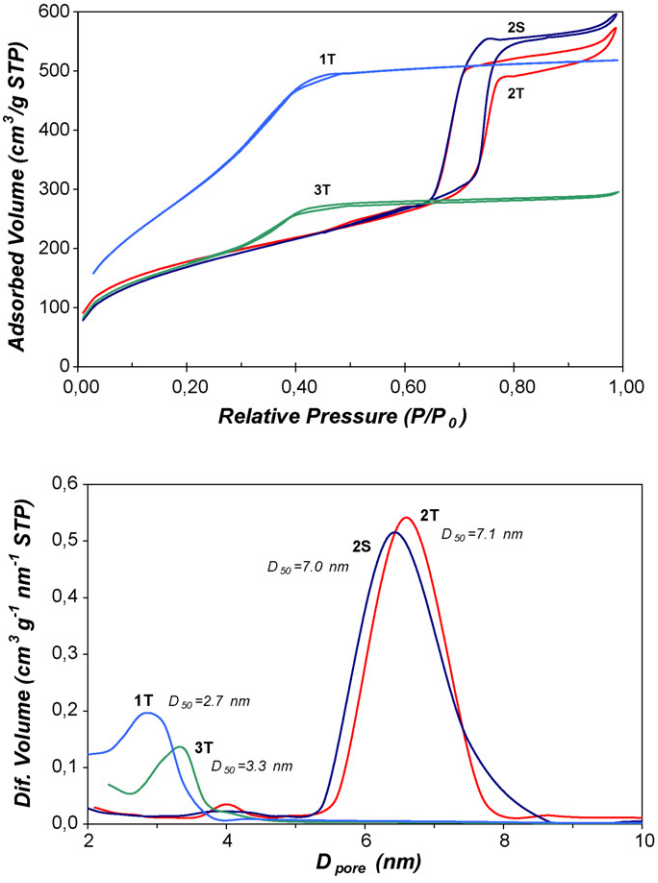

Fig. 1. Nitrogen adsorption–desorption isotherms, above, and pore size distribution curves (BJH), below, of Soxhlet-washed mesoporous silicas (**1T**, **2T**, **2S** and **3T**).

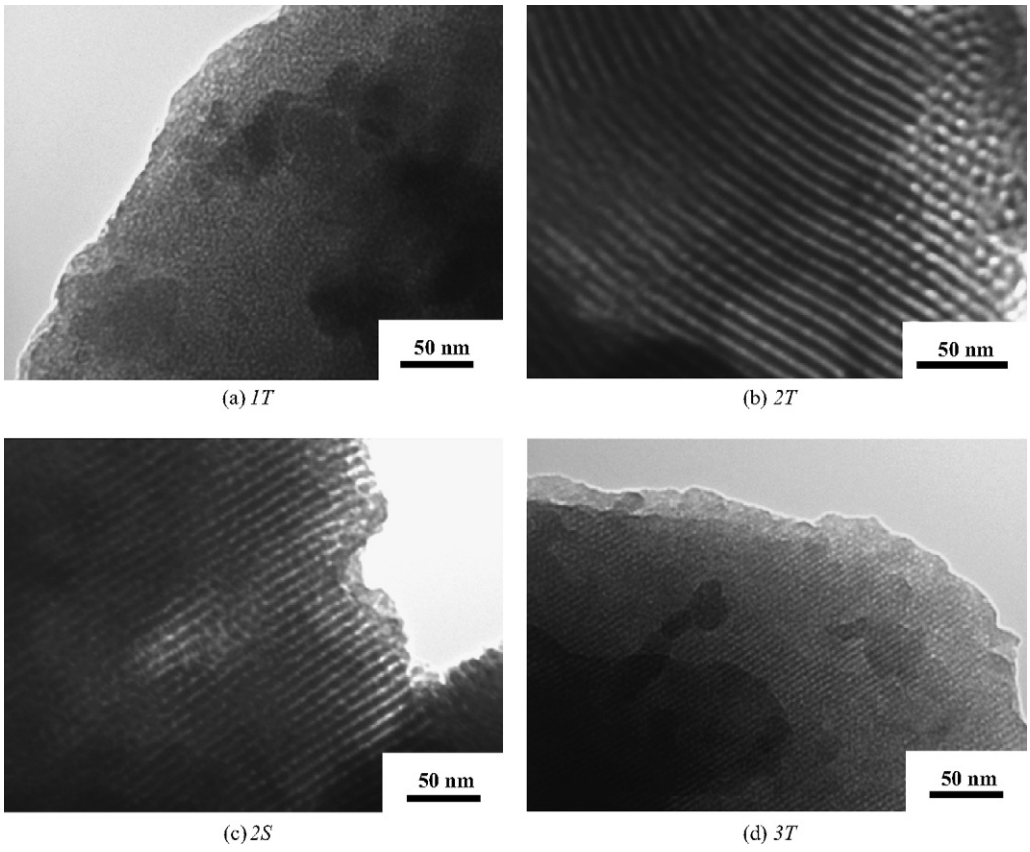

(a) *1T* (b) *2T*

(c) *2S* (d) *3T*

Fig. 2. Representative TEM images of Soxhlet-washed mesoporous silicas ((a) **1T**, (b) **2T**, (c) **2S** and (d) **3T**) employed as Si precursors for the production of Fe_2O_3–SiO_2 inclusion pigments (in the case of sample **2S**, see also the TEM detail included in Scheme 1).

(Fig. 2b and c); perfectly aligned (parallel) channels with sizes around 6–8 nm may be observed in both samples. Finally, mesoporous silica **3T** (Fig. 2d) also presents regularly spaced and organized mesoporous channels, but in this sample the mesopore sizes (below 5 nm) and wall thickness are considerably smaller.

In summary, the mesoporous silicas herein prepared with different templating agents exhibit in all cases considerably high surface areas (around 1114 m^2/g for **1T** and 630–650 m^2/g for the rest), and present a range of increasing average pore sizes (between 2.7 and 7.1 nm): **1T** (*ca.* 2.7 nm) ≤ **3T** (*ca.* 3.3 nm) < **2S** (*ca.* 7.0 nm) ≈ **2T** (*ca.* 7.1 nm). Samples **2T**, **2S** and **3T** possess also a well-ordered mesoscopic organization (hexagonal symmetry), being the mesopores of sample **1T** less organized (wormlike porosity).

3.2. XRD characterization of Fe_2O_3–SiO_2 nanocomposites

Structural information about the presence of crystalline samples in Fe-loaded silicas after the thermal treatment (calcination at 800 or 1000 °C) was obtained by XRD. The XRD patterns of representative nanocomposite samples fired 1000 °C-fired samples may be seen in Fig. 3 (the spectra obtained at 800 °C are not included for brevity reasons).

The XRD spectra of reference sample **R1** present at both temperatures (800 and 1000 °C) the typical diffraction peaks corresponding to SiO_2-quartz (used as Si precursor). In contrast, silica remains still amorphous at 800 °C in reference sample **R2** (prepared with colloidal silica), while it is already crystallized at 1000 °C as SiO_2-cristobalite (diffraction peaks of medium intensity). Remarkably, both reference samples also present at 800 and 1000 °C relatively intense XRD peaks associated to hematite (α-Fe_2O_3). Considering the peak width at medium height (Scherer formula), these peaks are associated to well-grown hematite crystals with considerably large crystallite sizes (above 100 nm).

Comparatively, hematite–silica nanocomposites prepared from mesoporous silicas by *direct calcination* (**A** samples) still contain amorphous silica, even after the firing treatment at 1000 °C (Fig. 3). The corresponding amorphous silica background at around 20–22° 2θ may be better appreciated in magnificated XRD patterns (not shown). Remarkably, all the XRD patterns present also peaks associated to well-grown hematite crystals (see the selected **1T-A** and **2S-A** patterns in Fig. 3). The intensity of hematite peaks is quite similar to that of reference samples, irrespective of the surface area and average pore size of mesoporous silicas. From these XRD patterns (using the Scherer formula) it is evident that these samples contain a considerable amount of hematite crystals having particle sizes (around 100 nm) larger than the pore sizes of pristine mesoporous silicas (2.7–7.1 nm). Thus, Fe-loading through the classical solid-state route does not enable to confine exclusively

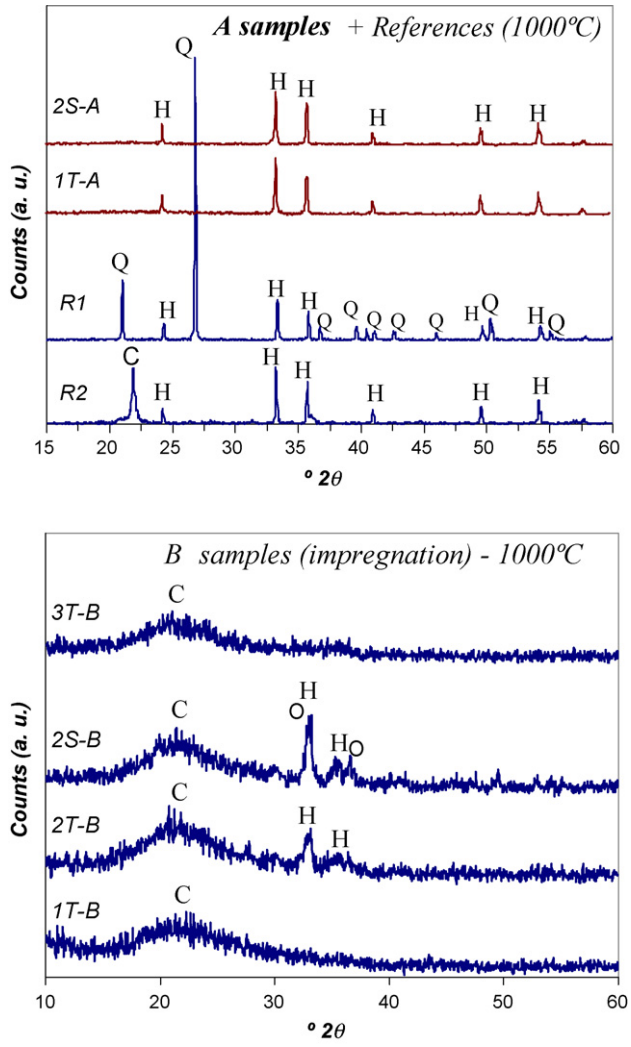

Fig. 3. XRD patterns of Fe-loaded samples after the calcination treatment at 1000 °C (references and representative **A** samples, above, and **B** samples below). Crystalline phases: C = SiO_2 (cristobalite), Q = SiO_2 (quartz), H = α-Fe_2O_3 (hematite), and O = orthorhombic Fe_2O_3 (residual phase in **2S-B** sample).

the growth of hematite particles inside the mesopores of host silicas, and larger hematite particles seem to grow also on external surfaces.

In contrast, XRD spectra of iron–silica nanocomposites (at 1000 °C) obtained by wet impregnation (**B** samples; see Fig. 3, below) show less intense or even absent iron oxide peaks. In the case of nanocomposite samples **1T-B** and **3T-B** (having smaller pore sizes, around 2.7–3.1 nm), the XRD spectra are completely free of iron oxide peaks. In contrast, composites obtained with mesoporous silicas **2T-B** and **2S-B** (with larger pore sizes, around 7.0–7.1 nm) present broad diffraction peaks of low intensity attributed to nanosized hematite (α-Fe_2O_3) crystals. The peaks intensity is much smaller than in references and **A** samples. In addition, the presence of orthorhombic Fe_2O_3 (O in Fig. 3) is also detected as residual phase accompanying hematite (specially in **2S-B** sample). The average hematite size calculated from the Scherer formula was around 20 and 33 nm for **2T-B** and **2S-B** samples, respectively. On the other hand, the broad band around 20–22° 2θ in all **B** samples is associated to the presence of amorphous silica, still on the first stages of cristobalite crystallization.

The smaller particle sizes of hematite crystals in impregnated **B** samples (not detected by XRD in **1T-B** and **3T-B**, due to its smaller size or also to its smaller amount) could be reflecting a more efficient confinement of hematite particles within the mesoporous system of amorphous silicas.[40,44] However, this must be further confirmed by electron microscopy characterization, as it is discussed below.

3.3. Morphology and composition characterization by electron microscopy

Representative SEM micrographs of 1000 °C-fired nanocomposites and reference samples are shown in Figs. 4 and 5 (backscattering detector was used to better appreciate the presence of chemical un-homogeneities). Regarding to calcined reference samples (**R1** and **R2**), SEM observations confirm in both cases an heterogeneous Fe distribution (see Fig. 4a and b, respectively). The clearly visible brighter regions correspond to Fe-enriched aggregates (indicated with ↑ Fe-% in SEM images), while the darker regions are Si-enriched (↓ Fe-%). Indeed, representative EDX mapping analyses and spectra of both reference samples (not shown) confirmed the higher Fe:Si ratio associated to the brighter regions. The average Fe_2O_3 content (wt%) estimated by EDX semiquantitative analyses in both samples was around 25–26 wt% (slightly lower than the theoretical 35 wt% Fe_2O_3 of the formulated composition, SiO_2–0.2Fe_2O_3).

Regarding to solid-state loaded **A** samples, SEM images show in general a more regular distribution of iron throughout the amorphous (cotton-like) silica aggregates (Fig. 4c–f). However, and similarly to reference samples, Fe-enriched (brighter) regions of bunchy nano-grained aggregates with relatively large sizes (*ca.* 1–5 μm) are still observed (see, *i.e.* the details of **2S-A** and **3T-A** in Fig. 4e and f). EDX analyses performed with 1000 °C-fired powders (not shown) confirmed some dispersion in the Fe:Si distribution, possessing the brighter aggregates a higher iron oxide content. The average Fe:Si molar ratio by EDX analyses was around 0.23:1 (*ca.* 21–26 wt% Fe_2O_3) for **1T-A** and **3T-A** samples, and a little bit higher for **2T-A** and **2S-A** (0.30:1; *ca.* 28 wt% Fe_2O_3).

In contrast, SEM images of impregnation **B** samples fired at 1000 °C (Fig. 5) exhibit a much more homogeneous morphology, without perceivable brightness/contrast differences throughout the grains (see, *i.e.* representative details of **1T-B** and **2S-B** nanocomposites in Fig. 5a and c). Elemental analyses (EDX) performed in different aggregates of **B** samples gave always a leveled Si:Fe ratio (representative EDX spectra are shown in Fig. 5b and d). This indicates a regular distribution of iron species throughout the amorphous silica matrix. Thus, the impregnation procedure employed in **B** samples seems to enable a higher microstructure control and a much more homogeneous encapsulation of iron species (in comparison to the solid-state route). Noteworthy, the average Fe:Si molar ratio was substantially lower in samples **1T-B** (*ca.* 0.05:1, or 6 wt% Fe_2O_3) and **3T-B** (*ca.* 0.06:1, or 7 wt% Fe_2O_3) than in **2T-B** (*ca.* 0.16:1,

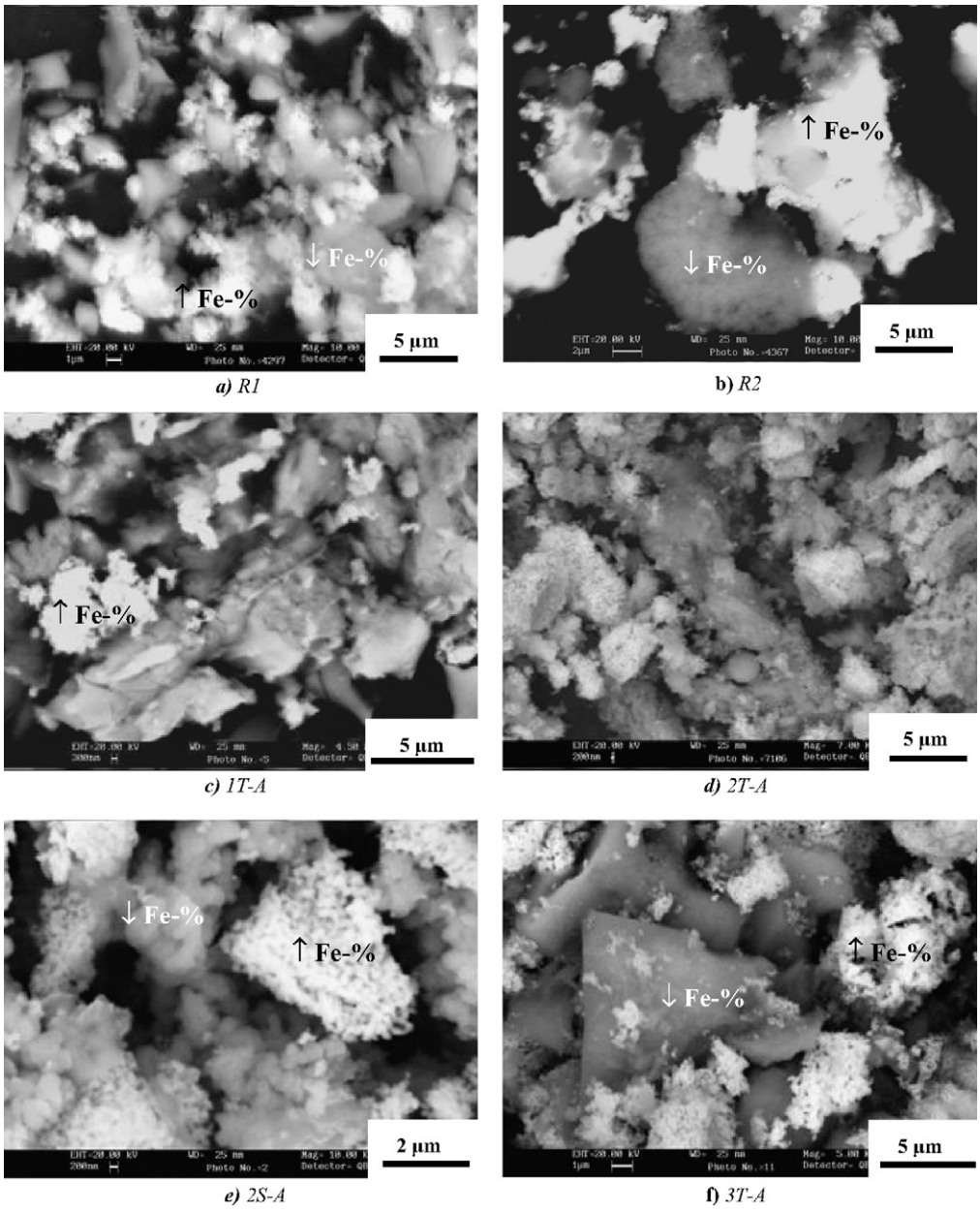

Fig. 4. Representative SEM images of Fe_2O_3–SiO_2 **A** samples (direct calcination route) after calcination at 1000 °C: (a) **R1** (reference with SiO_2-quartz), (b) **R2** (reference with colloidal SiO_2), (c) **1T-A** (C_{16}TAB-TEOS), (d) **2T-A** (P123-TEOS), (e) **2S-A** (P123-$Na_2Si_3O_7$), and (f) **3T-A** (Brij76-TEOS).

or 18 wt% Fe_2O_3) and **2S-B** (*ca.* 0.20:1, or 21 wt% Fe_2O_3), also in agreement with powder-XRD characterization (hematite XRD peaks were not detected in **1T-B** and **3T-B** samples). The average pore size of pristine mesoporous silicas was smaller in **1T** and **3T** samples (2.7–3.3 nm) than in **2T** or **2S** (7.0–7.1 nm). Thus, iron species seem to be incorporated in larger quantities by wet impregnation the higher the pore size. Also remarkably, the Fe_2O_3 loadings found in **2T-B** and **2S-B** samples (18–21 wt%) are considerably high, only slightly lower than in solid-state loaded **A** silicas (around 21–28 wt%).

Finally, TEM investigation of 1000 °C-fired nanocomposites (in areas with non-segregated hematite) enabled us to appreciate with much more insight the inclusion of iron oxide nanoparticles within the collapsed (sintered) mesoporous silica framework, and also their approximate particle size. TEM images of Fe–silica nanocomposites (see Figs. 6 and 7) show in general a stronger contrast than those of non-doped silica materials (Fig. 2), which can be attributed to the presence of the stronger scatterer/absorber iron in the silica framework. In the case of *solid-state loaded* samples (**A**), TEM observations show that iron oxide particles are regularly dispersed within the silica matrixes (Fig. 6a–f). Very interestingly, the existence of confinement effects on the growth of Fe_2O_3 particles within silica mesopores is confirmed by the correlation between the size of Fe_2O_3 particles and the pore size of pristine mesoporous silicas. In effect, from a visual inspection of TEM images the average

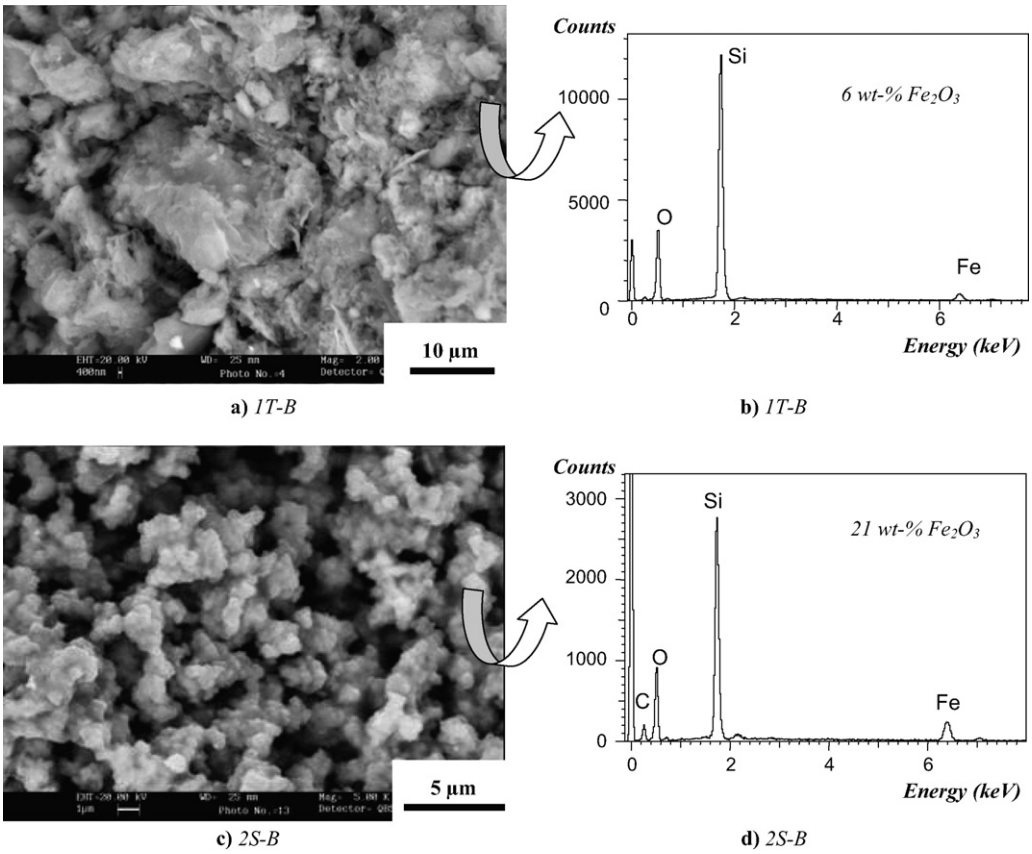

Fig. 5. Representative SEM images and EDX spectra of Fe_2O_3–SiO_2 **B** samples (impregnation or "incipient wetness" route) after calcination at 1000 °C: (a and b) **1T-B** (C_{16}TAB-TEOS); (c and d) **2S-B** (P123-$Na_2Si_3O_7$).

size of Fe_2O_3 particles may be estimated around (or below) 5 nm in **1T-A** sample (Fig. 6a and b), between 5 and 10 nm for **3T-A** sample (Fig. 6f), and around 10–20 nm for **2S-A** (not shown) and **2T-A** samples (Fig. 6c and d). Noteworthy, some reminiscences of original mesoporous channels may still be appreciated by TEM in some regions of **2S-A** and **2T-A** nanocomposites (see, *i.e.* TEM details of **2T-A** sample in Fig. 6c and e). Thus, the collapse and sintering of original mesopores was not fully achieved in these larger pore-sized silicas after calcination at 1000 °C.

Regarding to wet impregnated samples (**B**), TEM observation also confirmed a homogeneous distribution of iron oxide species (darker spots) throughout the silica matrixes in all samples (see selected TEM details in Fig. 7). The morphologies of Fe_2O_3 particles are mainly round-shaped, especially in samples **1T-B**, **2T-B** and **3T-B** (not shown), in accordance with the hexagonal (rhombohedral) symmetry of hematite particles. However, more elongated particles with higher aspect ratio are also appreciated (for instance, in the case of **2S-B**). These particles would correspond to the residual orthorhombic Fe_2O_3 also detected by powder-XRD (Fig. 3). The size of the included Fe_2O_3 particles is again around 5 nm in the case of **1T-B** (Fig. 7a) and **3T-B** samples (not shown), while in samples **2T-B** (Fig. 7b and c) and **2S-B** (Fig. 7e), comparatively, the average sizes may be estimated around 5–20 and 10–35 nm, respectively (it was around 20 nm for **2T-A** and **2S-A** samples). These values are in good agreement with the sizes calculated with the Scherer formula from the powder-XRD patterns (around 20 and 33 nm for **2T-B** and **2S-B**, respectively).

As a summary of the previous discussion, microstructure and composition characterization by SEM/EDX and TEM techniques confirm a higher iron oxide loading in solid-stated (**A**) samples (around 21–28 wt% Fe_2O_3) than in impregnated samples (around 6–7 wt% Fe_2O_3 for **1T-B** and **3T-B** samples, and *ca.* 18–21 wt% Fe_2O_3 for **2T-B** and **2S-B** samples). The presence of hematite-enriched aggregates is appreciated by SEM characterization in **A** samples, which also contain larger hematite particles (around 100 nm), presumably grown onto the external silica surfaces. In contrast, impregnated **B** samples exhibit a more regular and homogeneous distribution of smaller hematite nanoparticles. In these samples, iron species are more exclusively confined within the inner surfaces of the mesoporous silica matrix. TEM analyses of hematite–silica aggregates (at the local scale) confirm the inclusion of hematite nanoparticles with smaller sizes (below 5) in smaller pore-sized mesoporous silicas (**1T** and **3T**). In contrast, when using larger pore-sized mesoporous silicas (**2T** and **2S**), the resulting hematite nanoparticles present larger sizes (around 10–35 nm).

3.4. UV–vis-NIR and color characterization

Finally, and as the main objective of this study, the coloring performance as red ceramic pigments of the hematite–silica

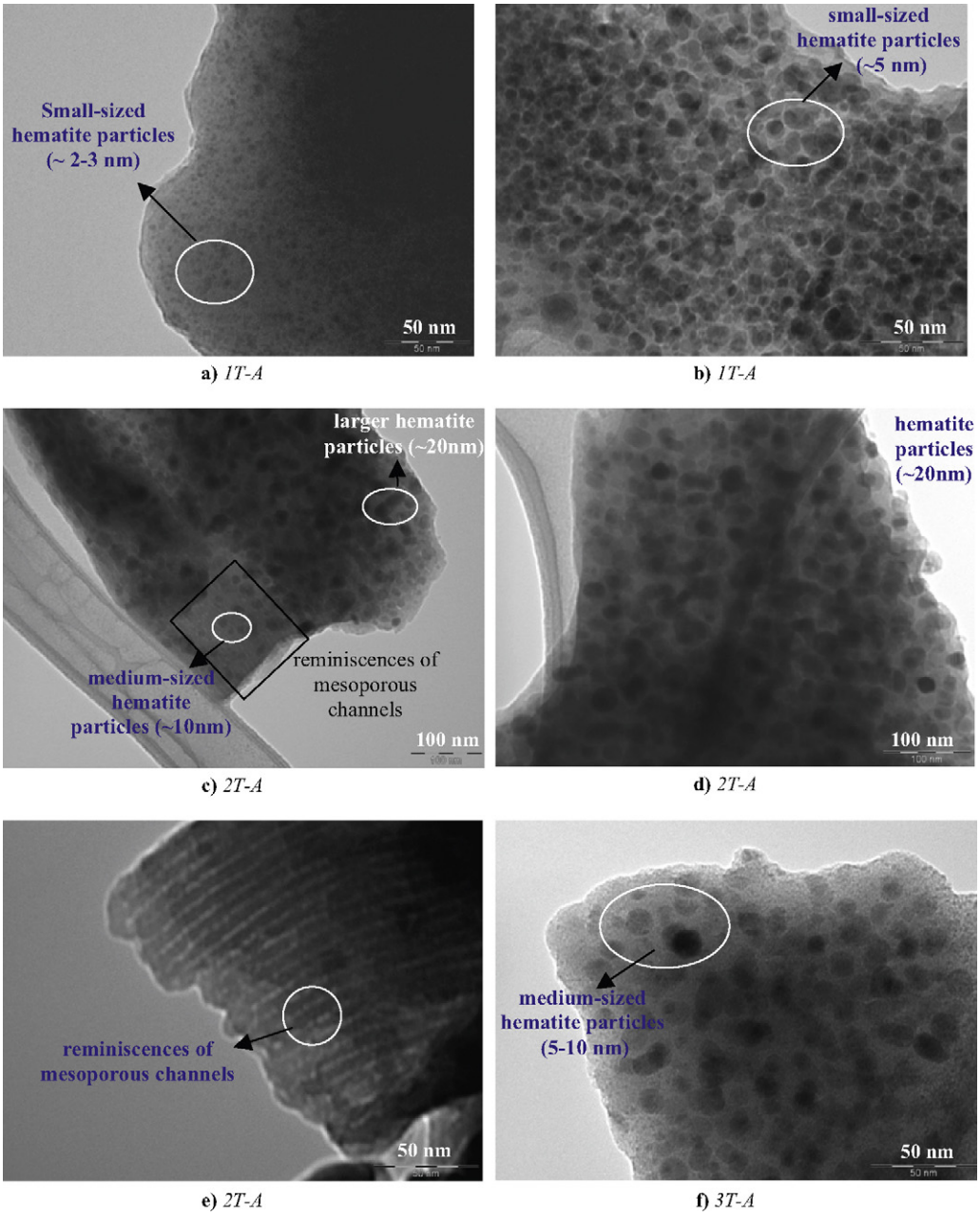

Fig. 6. Representative TEM images of Fe_2O_3–SiO_2 **A** samples ("direct calcination" route) after calcination at 1000 °C: **1T-A** (a and b), **2T-A** (c–e), and **3T-A** (f).

nanocomposites was finally evaluated by UV–vis spectroscopy and by colorimetric measurements (with both powder and enameled samples). As it was previously commented, the coloring properties of nanocomposites consisting of hematite nanoparticles included in mesoporous silicas have not yet been reported. The reddish color of hematite–silica inclusion pigments is associated to the presence of hematite crystals protected by amorphous silica grains. The intensity of the reddish color is directly proportional to the amount of efficiently protected hematite, with the appropriate size and morphology. A typical absorption spectrum of reddish bulk hematite (α-Fe_2O_3)[12] usually presents an intense charge transfer band centered at 290 nm due to iron–ligands interaction, followed by a band at 850 nm and two shoulders at 600–660 and 480–580 nm, that are attributed respectively to the spin-forbidden $^6A_{1g} \rightarrow {}^4T_{1g}$, $^6A_{1g} \rightarrow {}^4T_{2g}$, and $^6A_{1g} \rightarrow {}^4A_{1g}$ transitions of Fe^{3+} in octahedral environment (corundum structure of hematite).

All these features may be appreciated with a moderate intensity in the UV–vis spectra of enameled **A** samples fired at 800 °C (see Fig. 8, above). Interestingly, at 800 °C the Fe-loaded mesoporous silicas (**A** samples) produced slightly more intense reddish colors after the enameling process than the reference ceramic pigments (**R1** and **R2**). A representative picture of enameled references and **A** samples is shown in Fig. 9a. The better red color was corroborated by the stronger absorption band around 460–550 nm in the UV–vis spectra, as well as by the measured CIE-$L^*a^*b^*$ color parameters (see parameters at 800 °C in Table 3). In this colorimetric scale,[57] the yield of red

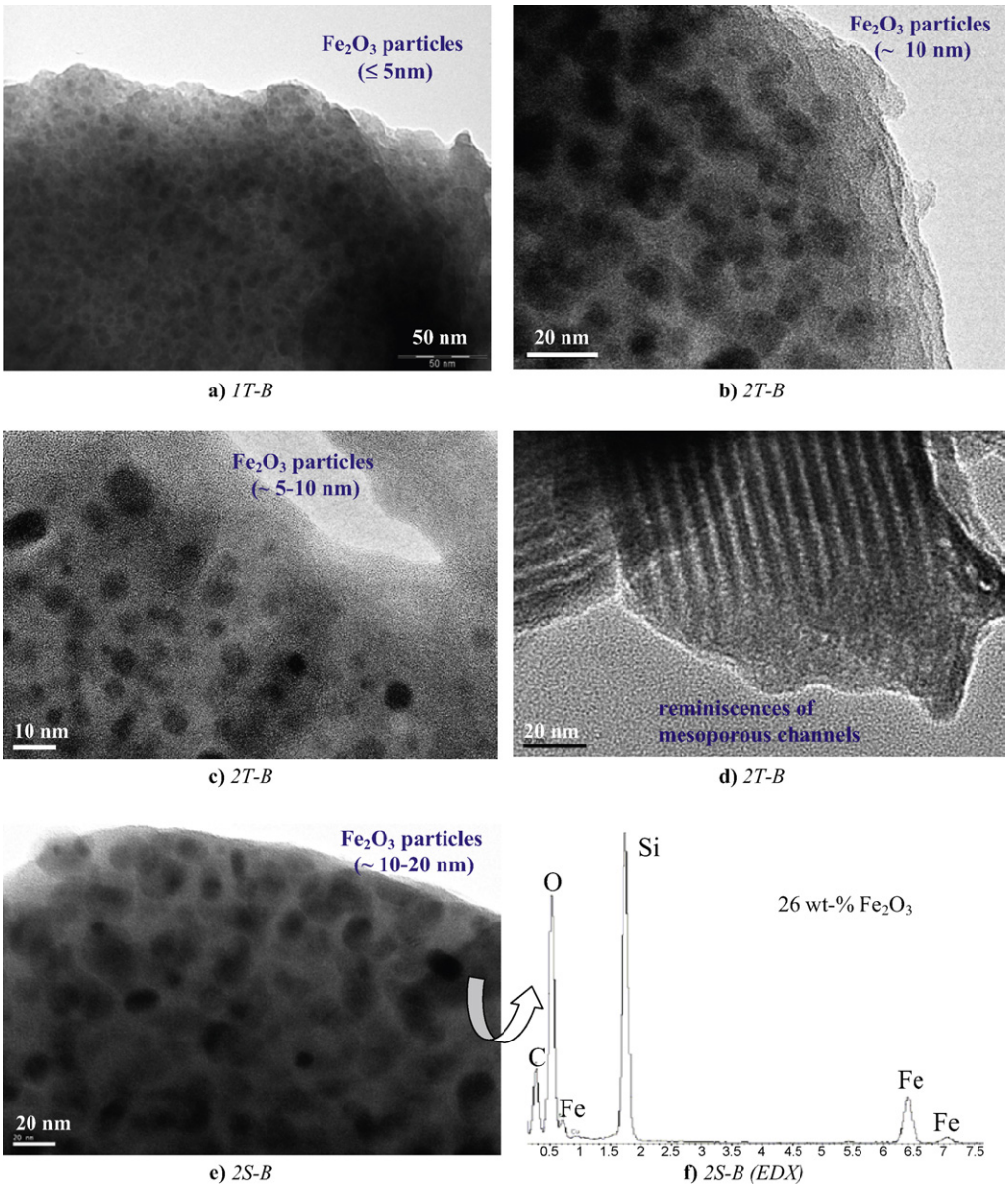

Fig. 7. Representative TEM images of Fe_2O_3–SiO_2 **B** samples (impregnation or "incipient wetness" route) after calcination at 1000 °C: **1T-B** (a), **2T-B** (b–d), and **2S-B** (e and corresponding EDX spectrum in f).

color is mainly governed by the parameter a^*: the more positive the a^* value, the redder the color hue. On the other hand, the color becomes more yellow the more positive the b^* value. Finally, the coordinate L^* gives us the lightness–brightness of the pigment (the lower L^*, the darker) as well as the intensity or saturation degree (the lower L^*, the more intense).

In effect, nanocomposite **A** samples (fired at 800 °C) exhibit slightly redder and more intense colorations than both ceramic references. Samples **A** present higher a^* values (around 16–20 against 14–15 for references), and lower L^* values (55–60 against 64–66), although they are also slightly more yellow according to the higher b^* values (34–37 against 31–34). As an additional and remarkable observation, there is no evident relationship between the pore size of pristine mesoporous silicas (or the size of included hematite nanoparticles) and the obtained red hues of nanocomposites **A** fired at 800 °C. The color

Table 3
Color parameters ($L^*a^*b^*$) of references (**R1** and **R2**) and "solid-state loaded" samples (**A**) fired at 800 °C.

800 °C	**R1**	**R2**	**3T-A**	**3T-A**	**2T-A**	**2S-A**
$L^*/a^*/b^*$ (powders)	54/22/15	49/26/25	50/20/14	50/14/15	52/16	51/16/17
$L^*/a^*/b^*$ (enameled)	66/**15**/31	64/**14**/34	60/**16**/34	56/**20**/37	55/**19**/37	56/**17**/36

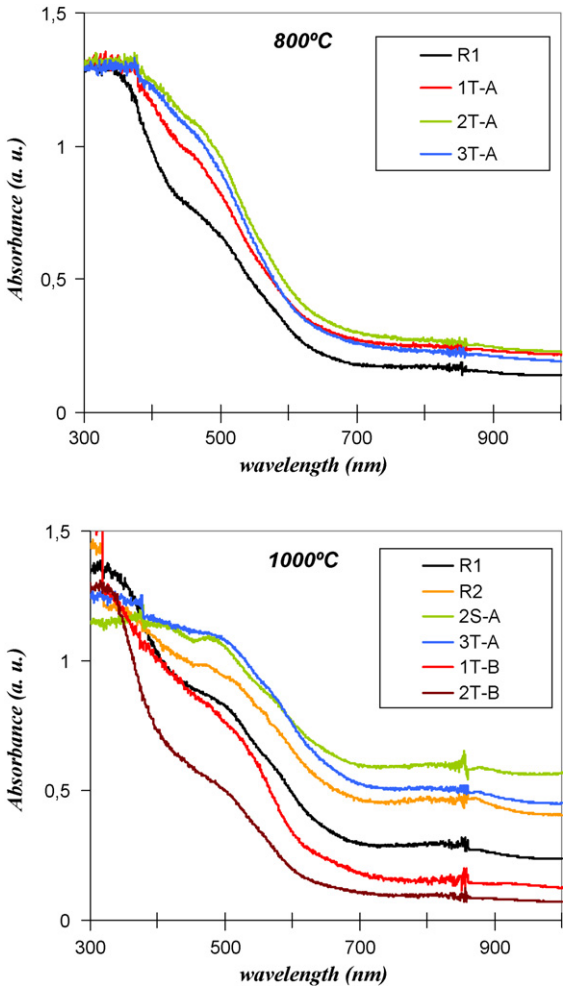

Fig. 8. UV–vis spectra of samples enameled with hematite–silica pigments fired at 800 °C (above; **A** samples) and 1000 °C (below; references **R1** and **R2**, and representative **A** and **B** samples).

of **A** nanocomposites seems therefore to be mostly influenced by the larger hematite particles (around 100 nm) non-efficiently protected by silica grains ("exogenous" hematite nanoparticles presumably grown onto external surfaces of silica mesopores). Indeed, nanocomposite **A** powders fired at 1000 °C and the corresponding enameled samples exhibited much darker or browner colorations. A comparison of the visual aspect of representative enameled samples (**2S-A** and **3T-A**) with pigments fired at 800 and 1000 °C is shown in the picture of Fig. 9b. It is generally accepted that darker brown colors are obtained when the hematite–silica pigment contains a higher amount of larger and non-protected hematite particles. In this case hematite can be more easily dissolved in the glaze or reduced to the darker magnetite (Fe_3O_4). In the UV–vis absorption spectra of enameled **A** samples at 1000 °C (Fig. 8, below), this effect is evidenced by the strongly increased absorption at higher wavelengths (from 600 nm), with respect to the 800 °C spectra. These browner colorations are also confirmed (see color parameters at 1000 °C in Table 4) by a strong decrease in the L^* (from 56–66 at 800 °C to 43–56 at 1000 °C) and b^* values (from 31–37 at 800 °C to 17–23 at 1000 °C), while the red a^* values exhibited only a slight decrease (from 14–20 to 12–16).

In contrast, hematite–silica nanocomposite pigments prepared by the incipient wetness procedure and fired at 1000 °C (**B** samples) produced even at this high temperature interesting reddish colorations (after the enameling process). Fig. 8 (below) shows also the UV–vis absorption spectra at 1000 °C of selected enameled **B** samples (**1T-B** representative of small pore-sized silicas, and **2T-B** representative of large pore-sized silicas), along with references and **A** samples. The UV–vis absorption spectra of both **B** samples (1000 °C-fired) present the typical bands of hematite, with a slightly reduced intensity between 450 and 600 nm with respect to **A** samples. However, these spectra have comparatively a much lower absorption at higher wavelengths (from 600 nm). Consequently, the selected **B** samples exhibit a more reddish and less brown color than solid-state samples (**A**). This could be attributed to the more homogeneous and efficient confinement of hematite nanoparticles onto the inner surfaces of pristine mesoporous silicas (confirmed by XRD, SEM/EDX and TEM characterization).

As a final observation, the color hue of non-enameled **B** powders (fired at 1000 °C) was slightly more reddish in **2T-B** (a^* value around 16) than in **1T-B** (a^* value around 10), in agreement with the higher iron loading accomplished in the former (18 wt%, against 6 wt%). However, after the enameling process the situation was reversed, and the best red hues were obtained with the lower pore-sized silica ($L^*/a^*/b^*$ parameters around 65/**18**/31 for **1T-B**, and around 69/**14**/31 for **2T-B**). This apparent contradiction could be explained by the expected reaction of the pigments with the glaze during enamel firing. In the case of **1T-B** nanocomposite (having smaller mesopores), a more efficient protection of hematite was accomplished due to the more extended sintering and collapse of the smaller mesopores during the firing treatment (as it was confirmed in TEM images). However, in the larger pore-sized nanocomposites (**2T-B** and **2S-B**) reminiscent mesoporous channels were still not fully sintered and accessible after the calcination at 1000 °C (see Fig. 7d, for **2T-B** sample). Thus, despite of the higher amount of Fe_2O_3, these particles can be more easily attacked by the glaze during the enamel firing (at 1085 °C) through this open porosity, and

Table 4
Color parameters ($L^*a^*b^*$) of references (**R1** and **R2**) and representative "solid-state loaded" samples (**3TA**, **2TA** and **2S-A**) and "wet impregnated" samples (**1T-B** and **2T-B**) fired at 1000 °C. The average hematite content (wt% Fe_2O_3) in the nanocomposite hematite–silica pigments measured by EDX is also included.

1000 °C	R1	R2	3T-A	2T-A	2S-A	1T-B	2T-B
$L^*/a^*/b^*$ (powders)	53/20/15	37/14/	46/14/10	49/16/13	48/17/13	59/**10**/22	58/**16**/24
$L^*/a^*/b^*$ (enameled)	56/**16**/23	46/**14**/18	43/**14**/17	44/**16**/21	44/**12**/17	65/**18**/31	69/**14**/31
Average (EDX) wt% Fe_2O_3	25%	26%	26%	28%	28%	6%	18%

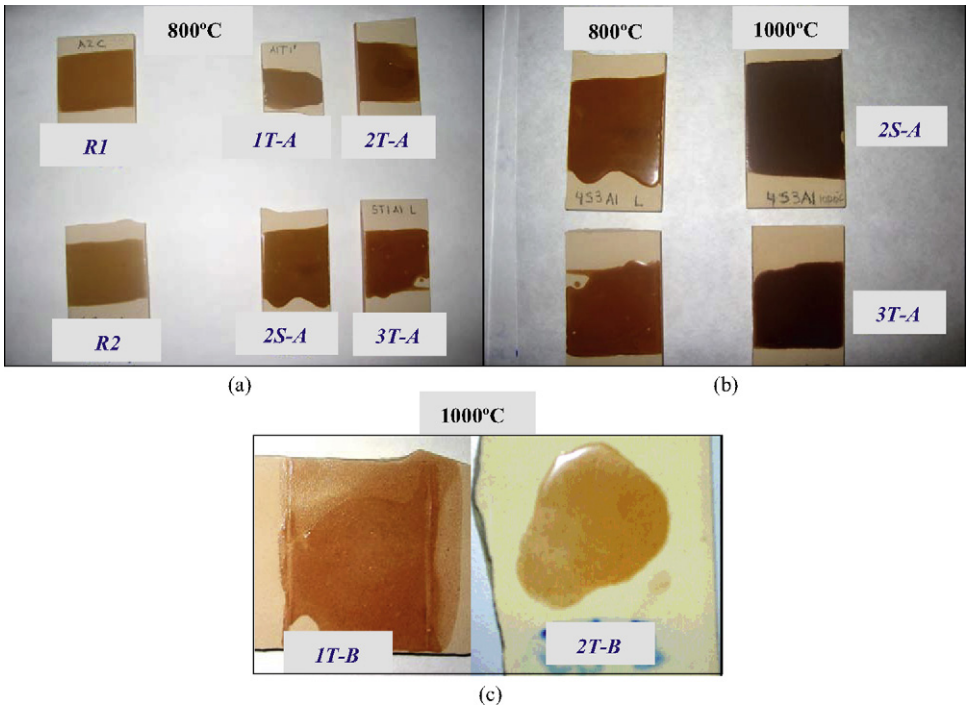

Fig. 9. Representative enameled samples (5% pigment in a transparent ceramic glaze): (a) references **R1** and **R2** and **A** samples ("direct calcination" route) fired at 800 °C; (b) comparison of samples **2S-A** and **3T-A** fired at 800 °C and 1000 °C, showing the change from reddish to dark-brown colorations when the firing temperature of the pigment is increased; and (c) comparison of representative "impregnation" **B** samples fired at 1000 °C (small pore-sized **1T-B**, and large pore-sized **2T-B**), with better preservation of the reddish coloration (than in **A** samples).

be consequently dissolved in the glaze, leading to poorer red hues.

4. Conclusions

The potential application as red ceramic pigments of hematite included in previously designed mesoporous silicas having controlled pore size and pore organization has been analyzed for the first time. The mesoporosity of precursor silicas has proven to have an important effect on both the efficient encapsulation of hematite nanoparticles and the performance as red ceramic pigments in the coloration of conventional transparent ceramic glazes.

As the most relevant results, the loading of iron species through wet impregnation (instead of the classical solid-state loading) leads to a much more efficient and homogeneous encapsulation of smaller hematite nanoparticles. Moreover, the size of hematite nanoparticles embedded in the silica matrixes can be partially controlled through confinement effects in the inner surfaces of silica mesopores. In comparison with reference samples prepared with other conventional (non-porous) silica sources, the obtained impregnated nanocomposites exhibit much more intense reddish colorations at 1000 °C. Thus, it is prevented the darkening effect at these temperatures (around 1000 °C) associated to the dissolution of non-protected, larger hematite particles. The best red shade was associated to nanocomposite inclusion pigments with smaller hematite nanoparticles, derived from smaller pore-sized silicas.

In summary, this work enlightens the possibility to control the final red hues and thermal stability of hematite–silica nanocomposites through confinement effects in mesoporous silicas with the appropriate surface areas and pore sizes. Current investigations are being carried out to better correlate the intensity of the reddish colorations with the size of hematite nanoparticles (and of the silica mesopores in which they are confined).

Acknowledgements

The authors thank the spanish "*Generalitat Valenciana*" (GV04B-697 and GV05/089 Projects) and "*Ministerio de Educación y Ciencia*" (Projects MAT2005-00507 and MAT2008-02893) for financial support. Moreover, the technical assistance provided by the Central Services of Scientific Instrumentation (SCIC) of the University Jaume I is also fully acknowledged. The authors are also grateful to V. Esteve Cano-Lopera for his helpful comments about XRD and TEM characterization.

Appendix A. Supplementary data

Supplementary data associated with this article can be found, in the online version, at doi:10.1016/j.jeurceramsoc.2009.07.018.

References

1. Monrós, G., García, A., Sorlí, S., Llusar, M., Calbo, J. and Tena, M. A., Heteromorphic pigment synthesis mechanisms. *Ceram. Acta*, 2002, **14**, 12–27.
2. Seabright, C. A. Ceramic Pigments, United States Patent 2,441,447 (11 May 1949).

3. DCMA, Classification and chemical description of the mixed metal oxide inorganic colored pigments. *Metal Oxides and Ceramic Color Subcommittee* (*2nd edition*). Dry Color Manufacturer's Ass. (DCMA), Washington, DC, 1982, pp. 1–68.
4. Llusar, M., Badenes, J. A., Calbo, J., Tena, M. A. and Monrós, G., Environmental and color optimisation of mineraliser addition in the synthesis of iron–zircon ceramic pigment. *Br. Ceram. Trans.*, 2000, **99**(1), 14–22.
5. Eppler, R. A., Zirconia-based colors for ceramic glazes. *Am. Ceram. Bull.*, 1977, **56**, 213–218.
6. Eppler, D. R. and Eppler, R. A., Analyzing the color of reddish glazes. *Ceram. Eng. Sci. Proc.*, 1996, **17**(1), 77–87.
7. Llusar, M., Forés, A., Badenes, J. A., Calbo, J., Tena, M. A. and Monrós, G., Color analysis of some cobalt-based blue pigments. *J. Eur. Ceram. Soc.*, 2001, **21**, 1121–1130.
8. Monrós, G., Carda, J., Tena, M. A., Escribano, P. and Alarcón, J., Synthesis of ZrO_2–V_2O_5 pigments by sol–gel methods. *Br. Ceram. Trans. J.*, 1991, **90**, 157–160.
9. Vicent, J. B., Llusar, M., Badenes, J., Tena, M. A., Vicente, M. and Monrós, G., Occlusion of chromophore oxides by sol-gel methods: application to the synthesis of hematite–silica red pigments. *Bol. Soc. Esp. Ceram. Vidr.*, 2000, **39**(1), 83–93.
10. Llusar, M., Calbo, J., Badenes, J. A., Tena, M. A. and Monrós, G., Synthesis of iron zircon coral by coprecipitation routes. *J. Mater. Sci.*, 2001, **36**, 153–163.
11. García, A., Calbo, J., Sorlí, S., Bedoya, D., Llusar, M., Badenes, J. *et al.*, Synthesis of hematite-zircon ceramic pigment by urea homogeneous coprecipitation. In *Proceedings of the International Symposium "Science for New Technology of Silicate Ceramics", CIMTEC 2002 (10th International Ceramics Congress and 3rd Forum on New Materials)*, 2002, pp. 287–298, Techna Srl (ISBN 88-86538-36-7).
12. García, A., Llusar, M., Badenes, J., Tena, M. A. and Monrós, G., Encapsulation of hematite in zircon by microemulsion and sol–gel methods. *J. Sol–Gel Sci. Technol.*, 2003, **27**, 267–275.
13. García, A., Llusar, M., Sorlí, S., Calbo, J., Tena, M. A. and Monrós, G., Effect of the surfactant and precipitant on the synthesis of pink coral by a microemulsion method. *J. Eur. Ceram. Soc.*, 2003, **23**, 1829–1838.
14. Bondioli, F., Ferrari, A. M., Leonelli, C. and Manfredini, T., Syntheses of Fe_2O_3/silica red inorganic inclusion pigments for ceramic applications. *Mater. Res. Bull.*, 1998, **33**, 723–729.
15. Hosseini-Zori, M., Taheri-Nassaj, E. and Mirhabibi, A. R., Effective factors on synthesis of the hematite–silica red inclusion pigment. *Ceram. Int.*, 2008, **34**, 491–496.
16. Hosseini-Zori, M., Bondioli, F., Manfredini, T. and Taheri-Nassaj, E., Effect of synthesis parameters on a hematite–silica red pigment obtained using a coprecipitation route. *Dyes Pigments*, 2008, **77**, 53–58.
17. American Ceramic Society, *Phase Diagrams for Ceramists*, *vol. I*., 1975, Fig. 87.
18. Cornell, R. M. and Schwertmann, U., *The Iron Oxides: Structure, Properties, Reactions, Occurrence and Uses*. VCH Verlag, Weinheim, 1996, pp. 573.
19. Costa, A. L., Matteucci, F., Dondi, M., Zama, I., Albonetti, S. and Baldi, G., Heterocoagulation-spray drying process for the inclusion of ceramic pigments. *J. Eur. Ceram. Soc.*, 2008, **28**, 169–176.
20. Ponce-Catañeda, S., Martínez, J. R., Ruiz, F., Palomares-Sánchez, S. and Domínguez, O., Synthesis of Fe_2O_3 species embedded in a silica xerogel matrix: a comparative study. *J. Sol–Gel Sci. Technol.*, 2002, **25**, 29–36.
21. Ponce-Catañeda, S., Martínez, J. R., Palomares-Sánchez, S., Ayala-Valenzuela, O. and Matutes-Aquino, J. A., Infrared spectroscopy analysis of oxyhydroxides as intermediate species in the formation of iron oxides-silica xerogels. *J. Sol–Gel Sci. Technol.*, 2003, **27**, 247–254.
22. Barrado, E., Rodríguez, J. A., Prieto, F. and Medina, J., Characterization of iron oxides embedded in silica gel obtained by two different methods. *J. Non-Cryst. Solids*, 2005, **351**, 906–914.
23. Soler-Illia, G. J., De, A. A., Sánchez, C., Lebeau, B. and Patarin, J., Chemical Strategies to DEAgn textured materials: from microporous and mesoporous oxides to nanonetworks and hierarchical structures. *Chem. Rev.*, 2002, **102**, 4093–4138.
24. Corma, A., From microporous to mesoporous molecular sieve materials and rheir use in catalysis. *Chem. Rev.*, 1997, **97**, 2373–2419.
25. Coppens, M. O., Sun, J. and Maschmeyer, T., Synthesis of hierarchical porous silicas with a controlled pore size distribution at various length scales. *Catal. Today*, 2001, **69**, 331–335.
26. Mann, S., Burkett, S. L., Davis, S. A., Fowler, C. E., Mendelson, N. H., Sims, S. D. *et al.*, Sol–gel synthesis of organized matter. *Chem. Mater.*, 1997, **9**, 2300–2310.
27. Imhof, A. and Pine, D. J., Ordered macroporous materials by emulsion templating. *Nature*, 1997, **389**, 948–951.
28. Ozin, G. A., Panoscopic materials: synthesis over 'all' length scales. *Chem. Commun.*, 2000, 419–432.
29. Abe, T., Tachibana, Y., Uematsu, T. and Iwamoto, M., Preparation and characterization of Fe_2O_3 nanoparticles in mesoporous silicate. *J. Chem. Commun.*, 1995, 1617–1618.
30. Yuan, Z. Y., Liu, S. Q., Chen, T. H., Wang, J. Z. and Li, H. X., Synthesis of iron-containing MCM-41. *J. Chem. Soc., Chem. Commun.*, 1995, 973–974 (the first report about Fe incorporation (in situ strategy) in a mesoporous MCM-41 silica).
31. Ohtaki, M., Inata, K. and Eguchi, K., Selective incorporation of inorganic precursors into the channels of MCM-41 by molecular assembly template as a hydrophobic carrier. *Chem. Mater.*, 1998, **10**, 2582–2584.
32. Wingen, A., Anastasievič, N., Hollnagel, A., Werner, D. and Schüth, F., Fe-MCM-41 as a catalyst for sulfur dioxide oxidation in highly concentrated gases. *J. Catal.*, 2000, **193**, 248–254.
33. Selvam, P., Dapurkar, S. E., Badamali, S. K., Murugasam, M. and Kuwano, H., Coexistence of paramagnetic and superparamagnetic Fe(III) in mesoporous MCM-41 silicates. *Catal. Today*, 2001, **68**, 69–74.
34. García, C., Zhang, Y., DiSalvo, F. and Wiesner, U., Mesoporous aluminosilicate materials with superparamagnetic γ-Fe_2O_3 particles embedded in the walls. *Angew. Chem. Int. Ed.*, 2003, **42**, 1526–1530.
35. Samanta, S., Giri, S., Sastry, P. U., Mal, N. K., Manna, S. and Bhaumik, A., Synthesis and characterization of iron-rich highly ordered mesoporous Fe-MCM-41. *Ind. Eng. Chem. Res.*, 2003, **42**, 3012–3018.
36. Gu, J., Shi, J., Xiong, L., Chen, H. and Ruan, M., A new strategy to incorporate highly dispersed nanoparticles into the pore channels of mesoporous silica thin films. *Micropor. Mesopor. Mater.*, 2004, **74**, 199–204.
37. Yang, H., Lu, Q., Gao, F., Shi, Q., Yan, Y., Zhang, F. *et al.*, One-step synthesis of highly ordered mesoporous silica monoliths with metal oxide nanocrystals in their channels. *Adv. Funct. Mater.*, 2005, **15**, 1377–1384.
38. Li, Y., Feng, Z., Lian, Y., Sun, K., Zhang, L., Jia, G. *et al.*, Direct synthesis of highly ordered Fe-SBA-15 mesoporous materials under weak acidic conditions. *Micropor. Mesopor. Mater.*, 2005, **84**, 41–49.
39. Julián-López, B., Boissière, C., Chanéac, C., Grosso, D., Vasseur, S., Miraux, S. *et al.*, Mesoporous maghemite-organosilica microspheres: a promising route towards multifunctional platforms for smart diagnosis and therapy. *J. Mater. Chem.*, 2007, **17**, 1563–1569.
40. Fröba, M., Köhn, R. and Bouffaud, G., Fe_2O_3 nanoparticles within mesoporous MCM-48 silica: in situ formation and characterization. *Chem. Mater.*, 1999, **11**, 2858–2865.
41. Iwamoto, M., Abe, T. and Tachibana, Y., Control of bandgap or iron oxide through its encapsulation into SiO_2-based mesoporous materials. *J. Mol. Catal. A*, 2000, **155**, 143–153.
42. Zheng, S., Gao, L., Zhang, Q.-H. and Guo, J.-K., Synthesis, characterization and photocatalytic properties of titania-modified mesoporous silicate MCM-41. *J. Mater. Chem.*, 2000, **10**, 723–727.
43. Mokaya, R. and Jones, W., Efficient post-synthesis alumination of MCM-41 using aluminium chlorohydrate containing Al polycations. *J. Mater. Chem.*, 1999, **9**, 555–561.
44. Schüth, F., Wingen, A. and Sauer, J., Oxide loaded ordered mesoporous oxides for catalytic applications. *Micropor. Mesopor. Mater.*, 2001, **44–45**, 465–476.
45. Sauer, J., Marlow, F., Spliethoff, B. and Schüth, F., Rare earth oxide coating of the walls of SBA-15. *Chem. Mater.*, 2002, **14**, 217–224.
46. Landau, M. V., Titelman, L., Vradman, L. and Wilson, P., Thermostable sulfated 2-4 nm tetragonal ZrO_2 with high loading in nanotubes of SBA-15: a superior acidic catalytic material. *Chem. Commun.*, 2003, 594–595.

47. Zhang, L., Papaefthymiou, G. C. and Ying, J. Y., Synthesis and properties of γ-Fe_2O_3 nanoclusters within mesoporous aluminosilicate matrices. *J. Phys. Chem. B*, 2001, **105**, 7414–7423.
48. Cannas, C., Musu, E., Musinu, A., Piccaluga, G. and Spano, G., Tuning of γ-Fe_2O_3 particle sizes by impregnation of mesoporous silica. *J. Non-Cryst. Solids*, 2004, **345–346**, 653–657.
49. Delahaye, E., Escax, V., El Hassan, N., Davidson, A., Aquino, R., Dupuis, V. *et al.*, Nanocasting: using SBA-15 silicas as hard templates to obtain ultrasmall monodispersed γ-Fe_2O_3 nanoparticles. *J. Phys. Chem. B*, 2006, **110**, 26001–26011.
50. Nakamura, T., Yamada, Y. and Yano, K., Novel synthesis of highly monodispersed γ-Fe_2O_3/SiO_2 and ε-Fe_2O_3/SiO_2 nanocomposite spheres. *J. Mater. Chem.*, 2006, **16**, 2417–2419.
51. Shi, K., Peng, L.-M., Chen, Q., Wang, R. and Zhou, W., Porous crystalline iron oxide thin films templated by mesoporous silica. *Micropor. Mesopor. Mater.*, 2005, **83**, 219–224.
52. Zhao, D., Huo, Q., Feng, J., Chemelka, B. F. and Stucky, G. D., Nonionic triblock and star diblock copolymer and oligomeric surfactant syntheses of highly ordered, hydrothermally stable, mesoporous silica structures. *J. Am. Chem. Soc.*, 1998, **120**, 6024–6636.
53. Brunauer, S., Emmet, P. H. and Teller, E., Adsorption of gases in multimolecular layers. *J. Am. Chem. Soc.*, 1938, **60**, 309–319.
54. Gregg, S. J. and Sing, K. S. W., *Adsorption, Surface Area and Porosity*. Academic Press, London, 1982.
55. Sing, K. S. W., Everett, D. H., Haul, R. A. W., Moscou, L., Pierotti, R. A., Rouquérol, J. *et al.*, Reporting physisorption data for gas/solid systems with special reference to the determination of surface area and porosity. *Pure Appl. Chem.*, 1985, **57**, 603–619.
56. Barret, E. P., Joyner, L. G. and Halenda, P. H., The determination of pore volume and area distributions in porous substances. I. Computations from nitrogen isotherms. *J. Am. Chem. Soc.*, 1951, **73**, 373–380.
57. CIE, Recommendations on Uniform Color Spaces, Color Difference Equations, Psychometrics Color Terms. Supplement No. 2 of CIE Publ. No. 15 (E-1.3.1) 1971, Bureau Central de la CIE, Paris, 1978.